Counterion Distribution Surrounding Spherical Nucleic Acid–Au Nanoparticle Conjugates Probed by Small-Angle X-ray Scattering

Sumit Kewalramani,[†] Jos W. Zwanikken,[†] Robert J. Macfarlane,[‡,⊥] Cheuk-Yui Leung,[§,∥] Monica Olvera de la Cruz,[†,‡] Chad A. Mirkin,[†,‡] and Michael J. Bedzyk*[,†,§]

[†]Department of Materials Science and Engineering, [‡]Department of Chemistry, and [§]Department of Physics and Astronomy, Northwestern University, Evanston, Illinois 60208, United States. [⊥]Present address: R.J.M.: Division of Chemistry and Chemical Engineering and Applied Physics Department, California Institute of Technology, Pasadena, California 91125, United States. [∥]Present address: C.-Y.L.: Biogen Idec, Cambridge, Massachusetts 02142, United States.

ABSTRACT The radial distribution of monovalent cations surrounding spherical nucleic acid–Au nanoparticle conjugates (SNA-AuNPs) is determined by *in situ* small-angle x-ray scattering (SAXS) and classical density functional theory (DFT) calculations. Small differences in SAXS intensity profiles from SNA-AuNPs dispersed in a series of solutions containing different monovalent ions (Na^+, K^+, Rb^+, or Cs^+) are measured. Using the "heavy ion replacement" SAXS (HIRSAXS) approach, we extract the cation-distribution-dependent contribution to the SAXS intensity and show that it agrees with DFT predictions. The experiment–theory comparisons reveal the radial distribution of cations as well as the conformation of the DNA in the SNA shell. The analysis shows an enhancement to the average cation concentration in the SNA shell that can be up to 15-fold, depending on the bulk solution ionic concentration. The study demonstrates the feasibility of HIRSAXS in probing the distribution of monovalent cations surrounding nanoparticles with an electron dense core (*e.g.*, metals).

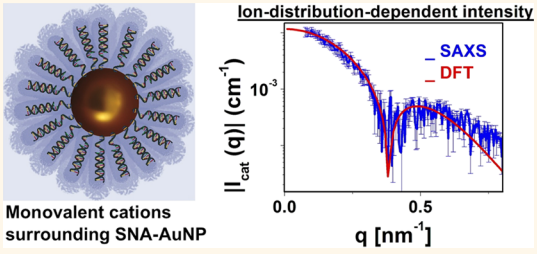

KEYWORDS: counterion distribution · DNA-coated gold nanoparticles · small-angle X-ray scattering · density functional theory

Spherical nucleic acid–Au nanoparticle conjugates (SNA-AuNPs) consist of spherical Au nanoparticles, each coated with a dense monolayer of synthetic oligonucleotides.[1−4] SNA-AuNPs have properties that are remarkably different from linear nucleic acids, making them useful in biodiagnostics and therapeutics. These properties include a high binding affinity for complementary nucleic acids,[2,3,5] enhanced resistance to enzymatic degradation as compared to molecular probes of the same sequence,[2,3,6,7] and the ability to enter over 50 different cell types without the need for transfection agents.[2,3,6] The origins of these properties have been linked, in part, to the salt-rich environment of the SNAs that screens the electrostatic repulsion between the adjacent negatively charged nucleic acids (see Figure 1A). Indeed, the dense loading of the oligonucleotides on the surface of the Au nanoparticles has been hypothesized to lead to a local environment that stabilizes duplexed nucleic acids and yields the highly cooperative melting behavior uniquely associated with SNAs.[5,8] Similarly, the enhanced resistance of SNA-AuNPs to nuclease degradation is attributed in part to the high local cation concentration of SNA-AuNPs,[2,3,7] which is believed to inhibit the activity of certain nucleases. From the above, it is evident that, to understand the effects of salts on the SNA-AuNP characteristics, the first step is to decipher the distribution of counterions surrounding SNA-AuNPs. Recently, classical density functional theory (DFT) calculations and molecular dynamics (MD) simulations were carried out to determine the distribution of monovalent and divalent cations surrounding Au nanoparticles capped with rigid polyelectrolytes, such as double-stranded (ds)-DNA.[9] However, to date, there has been no experimental study of the distribution of cations surrounding SNA-AuNPs. Herein, we report a small-angle X-ray scattering (SAXS) investigation

* Address correspondence to bedzyk@northwestern.edu.

Received for review October 1, 2013 and accepted November 19, 2013.

Published online November 19, 2013
10.1021/nn405109z

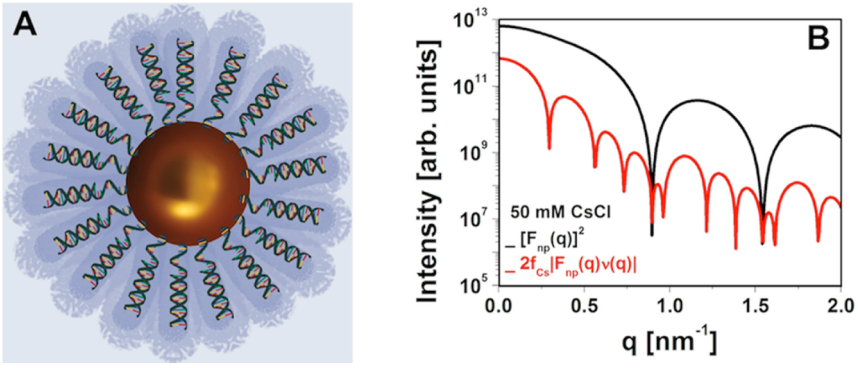

Figure 1. (A) SNA-AuNP schematic showing the counterion cloud screening the charge of the DNA grafted to a Au nanoparticle. The schematic shows the single-stranded and double-stranded DNA sections used in our theoretical models and experiments. The DNA strands consist of a 10-base single-stranded spacer (A_{10}) followed by an 18 base-pair duplex. The DNA strands are tethered to the Au core *via* propyl thiol linkers. (B) Model SAXS intensity calculations for the case of SNA-AuNPs in 50 mM CsCl showing eq 1 contributions from the dominant cation-independent term (top black line) and weaker cation-distribution-dependent term (red line).

of the distribution of monovalent counterions surrounding SNA-AuNPs.

Small-angle X-ray scattering (SAXS) is an obvious *in situ* probe for characterizing the counterion distribution with nanometer-resolution. Since X-rays scatter from electrons, the key challenge is to distinguish the very weakly scattering counterions from the very strongly scattering Au cores. In principle, the anomalous SAXS (ASAXS) approach is ideal for quantifying the counterion distribution around nanometer-scale colloidal particles in solutions[10−15] because of the possibility of extracting the ion distribution in a model-independent manner.[12,13] However, due to the extremely strong scattering from the electron-dense Au cores, ASAXS proved to be ineffective at sensing the much weaker scattering counterions surrounding the SNA-AuNPs [Figure S1 and text in Supporting Information (SI)].

An alternative to ASAXS is the "isomorphous heavy ion replacement" SAXS (HIRSAXS) approach, as this technique is significantly more sensitive to the ion distribution surrounding charged nanoparticles. For the present study on distribution of monovalent cations surrounding SNA-AuNPs, HIRSAXS is 5-fold more sensitive than ASAXS (SI). However, HIRSAXS requires the assumption that the ion distribution only depends on the ion valency and not the ion size.[10] For monovalent cations surrounding short oligonucleotides, this assumption has been validated by previous SAXS experiments,[10] where the counterion profiles extracted *via* the ASAXS and the HIRSAXS were found to be identical. Using DFT, we show (Figure S2, SI) that this "ion size-effect" assumption will also work for our present study of SNA-AuNPs.

We apply HIRSAXS to extract the radial distribution of monovalent cations [$n_+(r)$] surrounding SNA-AuNPs by measuring the changes in scattered intensity patterns from SNA-AuNPs dispersed in a series of solutions that contain different monovalent ions (Na^+, K^+, Rb^+, or Cs^+), ranging from low-Z to high-Z. We note that the cation distribution has an angular as well as a radial dependence.[9] However, for simplicity, the cation distribution is considered to depend only on radial distance from the Au core center due to the relatively low spatial resolution for cation distribution in our experiments. Furthermore, the approach is validated by a reasonable match between the experimental cation-distribution-dependent SAXS intensities and those derived from DFT-based calculations with angular-averaged cation densities, as demonstrated below.

For a counterion M^+, the scattered intensity from SNA-AuNP counterions, above the scattering from the salt solution [$\Delta I_M(q)$] can be approximated as a sum of two components (Figure 1B and SI).

$$\Delta I_M(q) = [F_{np}(q)]^2 + 2\Delta f_M[F_{np}(q)\nu(q)]$$
$$= [F_{np}(q)]^2 + \Delta f_M I_{cat}(q) \quad (1)$$

Here, q (= $4\pi \sin\theta/\lambda$) is the modulus of the scattering vector, 2θ is the scattering angle, and λ is the X-ray wavelength. In eq 1, the first term, $[F_{np}(q)]^2$, is cation-independent and is related to the scattering from the SNA-AuNPs, water, and the salt anions (SI). The second term, $2\Delta f_M[F_{np}(q)\nu(q)]$, incorporates the cation radial distribution profile as well as the cation identity M^+ (= Na^+, K^+, Rb^+, or Cs^+). The sought-after cation distribution profile, $n_+(r)$, is embedded in $\nu(q)$, which is the Fourier transform of the excess cation density [$n_+(r) - n_s$] surrounding the spherically symmetric SNA-AuNP. Here, n_s is the cation density in the bulk solution, far from the SNA-AuNPs.

$$\nu(q) = 4\pi \int_0^\infty [n_+(r) - n_s]\frac{\sin(qr)}{qr} r^2 dr \quad (2)$$

Finally, for a given cation, the renormalized contrast (or the effective number of electrons per cation) in water is

$$\Delta f_M = Z_M - \rho_w V_M \quad (3)$$

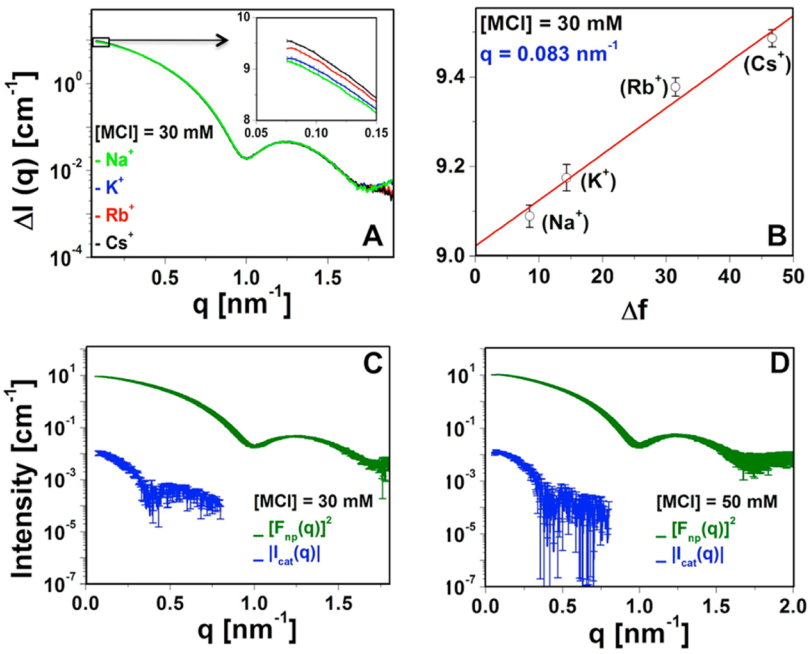

Figure 2. Extraction of cation-independent $[F_{np}(q)]^2$ and cation-profile-dependent $I_{cat}(q)$ intensities from SAXS measurements. (A) The processed SAXS intensity profiles $\Delta I_M(q)$ for 70 nM SNA-AuNPs in 30 mM MCl (M = Na, K, Rb, Cs). The inset shows the cation-dependent differences in the SAXS intensities at low q. (B) Linear fit to the SAXS intensities ΔI_M *vs* Δf_M at $q = 0.083$ nm^{-1}. Similar fits were performed at all q values corresponding to the data in A, and the result of the extraction is shown in C. (D) The extracted profiles $[F_{np}(q)]^2$ and $I_{cat}(q)$ for 80 nM SNA-AuNPs in 50 mM MCl.

Here, ρ_w is the electron density for water (334 e/nm^3), and V_M is the volume of the water that is displaced by the cation M^+. In the present study, V_M is calculated from tabulated Pauling radii. The computed Δf_M are 8.51, 14.32, 31.46, and 46.62 for $M^+ = Na^+$, K^+, Rb^+, and Cs^+, respectively (Table S1, SI). In our HIRSAXS analysis, the cation-independent and the cation-distribution-dependent intensities, *i.e.*, $[F_{np}(q)]^2$ and $I_{cat}(q)$ eq 1, are separated out *via* linear fits to the four (Δf_M, ΔI_M) data points at each q. $[F_{np}(q)]^2$ and $I_{cat}(q)$ correspond to the intercepts and slopes of such fits. Note that $I_{cat}(q)$ does not contain the cation specific factor Δf_M. Therefore, it depends on the cation distribution, but not on the cation species.

RESULTS AND DISCUSSION

The feasibility of HIRSAXS in sensing the counterion cloud structure surrounding SNA-AuNPs is suggested by simplified calculations (SI) for SNA-AuNPs in 30 and 50 mM salt solutions, which are the two concentrations studied in the experiments. Figure 1B shows the results of one such SAXS calculation for SNA-AuNPs in 50 mM Cs^+ and illustrates that the dominant intensity contribution, namely, the cation-independent $[F_{np}(q)]^2$ term in eq 1, exhibits larger periods for the sharp intensity oscillations than the second and weaker term $2\Delta f_{Cs}|F_{np}(q)\nu(q)|$, which depends on the counterion distribution. As evident from the expression for the cation-distribution-dependent intensity, the shift of the minima positions to lower q is due to $[\nu(q)]$. This is because the positions of the sharp minima for $[F_{np}(q)]$ must be the same as that for $[F_{np}(q)]^2$ and are primarily determined by the Au core size. Note, the lower q positions for the minima implies a larger radial spread. Therefore, the above-mentioned changes in the minima positions reflect that Au cores have a much smaller radial extent than the counterions. Further, at $q = 0$, the term $2\Delta f_{Cs}|F_{np}(q)\nu(q)|$ contributes 9.5% to the overall SAXS intensity (Figure 1B). The corresponding values for Rb^+, K^+, and Na^+ are 6.5%, 3.1%, and 1.9%, respectively. The small contributions due to the cations to the overall SAXS intensities again highlight the challenge in extracting the cation distribution surrounding SNA-AuNPs. Nevertheless, the above observations imply that, when the ion in the solution is changed from Na^+ to Rb^+ or Cs^+, the SAXS intensity can change by ~5% or ~8.5%, respectively. We show that such changes are measurable above the counting statistics uncertainties for our experiment and can be used to quantitatively examine the radial distribution of cations surrounding the SNA-AuNPs.

Figure 2A shows the four processed SAXS intensity profiles for 70 nM SNA-AuNPs in 30 mM MCl solutions, where M represents Na, K, Rb, or Cs. The intensity profiles are not visually separable unless the vertical scale is greatly magnified (inset, Figure 2A). This experimentally demonstrates how scattering from the Au cores dominates the overall SAXS pattern. Based on SAXS from a solid homogeneous sphere,[16] the position for the first minima at $q_{min} \sim 1.0$ nm^{-1} corresponds to a Au core radius of $R \sim 4.5/q_{min} \sim 4.5$ nm. The qualitative features of the SAXS scattering from SNA-AuNP-counterion

systems are independent of the cation species in the solution. However, one can see from the inset in Figure 2A that, at low q, the SAXS intensities follow the sequence $\Delta I_{Cs} > \Delta I_{Rb} > \Delta I_{K} > \Delta I_{Na}$. These cation-dependent differences are qualitatively consistent with the linear dependence of SAXS intensities ΔI_M on the cation scattering power Δf_M (eq 1). This suggests that, over the measured q range (Figure 2A), the cation-independent and cation-distribution-dependent SAXS intensities, $[F_{np}(q)]^2$ and $I_{cat}(q)$, can be separated out *via* the linear fit procedure outlined above. Figure 2B shows an example of such a fit to the ΔI_M *vs* Δf_M data at $q = 0.083$ nm^{-1}, and Figure 2C−D show the extracted $[F_{np}(q)]^2$ and $|I_{cat}(q)|$ profiles for 70 nM SNA-AuNPs in 30 mM MCl and 80 nM SNA-AuNPs in 50 mM MCl, respectively (for further details see "Data processing" section in SI). For both samples, the $|I_{cat}(q)|$ profiles are shown for $q \leq 0.8$ nm^{-1} because above this q, the uncertainties are typically 70−100% of the extracted $|I_{cat}(q)|$ values, as more readily evident in Figure 2D (a more extended range is shown in Figure S3).

Visual inspection of the cation-distribution-dependent SAXS intensity $|I_{cat}(q)|$ (Figure 2C−D) reveals that HIRSAXS is sensitive to the distribution of counterions surrounding SNA-AuNPs. To elaborate, the first minimum in $|I_{cat}(q)|$ is at $q \sim 0.38$ nm^{-1}, which is significantly smaller than the position of the first sharp minima at $q \sim 1.0$ nm^{-1} for $[F_{np}(q)]^2$. As discussed above, the minimum position is inversely related to the spatial extent. Therefore, this experimentally demonstrates that the radial extent of cation distribution far exceeds the size of the Au core.

Quantitative details of the cation distribution profiles $n_+(r)$ could be directly obtained from the SAXS-extracted profiles (Figure 2C−D), if the SNA-AuNPs were monodispersed in size. Specifically, the excess cation density $[n_+(r) - n_s]$ is the Fourier transform of $I_{cat}(q)/2[F_{np}(q)^2]^{1/2}$. However, as is typical with synthetic nanoparticles, the SNA-AuNPs are polydispersed (Figure 3). Therefore, a two-step approach is used to determine the cation distribution profile. First, we quantify the SNA-AuNP size distribution and the Au-core-size-dependence of oligonucleotides per SNA-AuNP $[N_{DNA}(R)]$,[17,18] which directly influences the cation distribution. These model SNA-AuNP parameters are used to derive the Au-size-dependent $F_{np}(q)$, required for the calculation of the theoretical polydispersity-averaged $I_{cat}(q) = 2\langle F_{np}(q)\nu(q)\rangle$, which will be compared to our HIRSAXS-measured $I_{cat}(q)$. For polydispersity-averaging, the Fourier transforms of the excess cation distribution $[\nu(q)]$ are obtained from DFT for the appropriate range of Au core sizes, as described below (see also Materials and Methods).

To determine SNA-AuNP structural characteristics, HIRSAXS-derived cation-independent intensities $[F_{np}(q)]^2$ are fitted to a model based on Au core sizes following a Schulz distribution (Figure 3, inset).[16] The contribution from the SNA shell to $[F_{np}(q)]^2$ is calculated by treating oligonucleotide strands as radially extended cylindrical

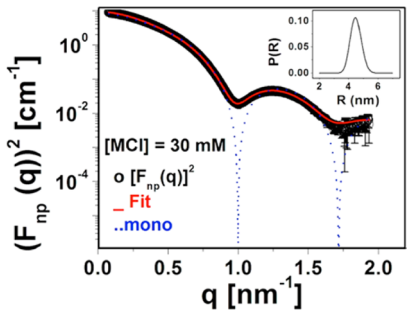

Figure 3. Characterization of the SNA-AuNP structure. HIRSAXS-extracted $[F_{np}(q)]^2$ for SNA-AuNPs in 30 mM MCl (black circles) and the corresponding best fit (solid red line) based on Schulz distribution (inset) for Au core sizes. For comparison, $[F_{np}(q)]^2$ corresponding to monodisperse Au cores with $R = 4.5$ nm is shown (dotted blue line).

TABLE 1. SNA-AuNP Structural Characteristics[a]

[MCl]	$\langle R\rangle$ (nm)	% PD	t_{DNA} (nm)	ρ_{DNA} (e/nm^3)	N_{DNA}
30 mM	4.49	8.4	8.22	446	55
50 mM	4.52	8.7	8.16	424	55

[a] The number of oligonucleotides per SNA-AuNP N_{DNA} is listed for the mean size of the Au core.

rods. Each rod has a 1.0 nm radius, a length equivalent to the SNA shell thickness t_{DNA}, and a fixed electron density, ρ_{DNA}. To account for salt concentration-dependent changes in the oligonucleotide conformation, t_{DNA} and ρ_{DNA} are fitted independently for the case of SNA-AuNP in 30 and 50 mM MCl. Finally, for each Au core size, a maximum DNA loading is assumed (for further details on the model see SI). By fitting the previously published data[17] for the minimum footprint of the oligonucleotide on the Au core (Figure S4A, SI), it can be shown that the number of oligonucleotides per SNA-AuNP is $N_{DNA}(R) = 4\pi R^{3/2}/2.19$ (Figure S4B, SI), where R is the radius of the Au core in nanometers. The best-fit parameters for SNA-AuNPs in 30 and 50 mM MCl solutions are summarized in Table 1. As can be seen from Table 1, no large changes in the SNA-AuNP structural characteristics occur in going from 30 to 50 mM salt concentration. The key results are that the mean Au core size $\langle R\rangle \sim 4.5$ nm is consistent with the size of the Au core derived from the position $q_{min} \sim 1.0$ nm^{-1} in the SAXS profile. The polydispersity (PD) is ~8.5%. Further, the best-fit values for the oligonucleotide electron densities ($\langle\rho_{DNA}\rangle \sim 435$ e/nm^3) are consistent with previously published values for the electron densities of proteins.[19] Similarly, the thickness for the oligonucleotide shell ($t_{DNA} \sim 8.2$ nm) corresponds approximately to the previous SAXS-derived average rise per base or base pair of $d_{DNA} \sim 0.26$ or 0.28 nm observed in the DNA-programmed crystalline assemblies of spherical or planar Au nanoparticles.[20,21] Therefore, the fit-derived ρ_{DNA} and t_{DNA} are reasonable as effective parameters for the oligonucleotides that cap the Au core.

Figure 4A shows the classical density functional theory (DFT)-derived distribution of Na^+ $[n_{+DFT}(r)]$

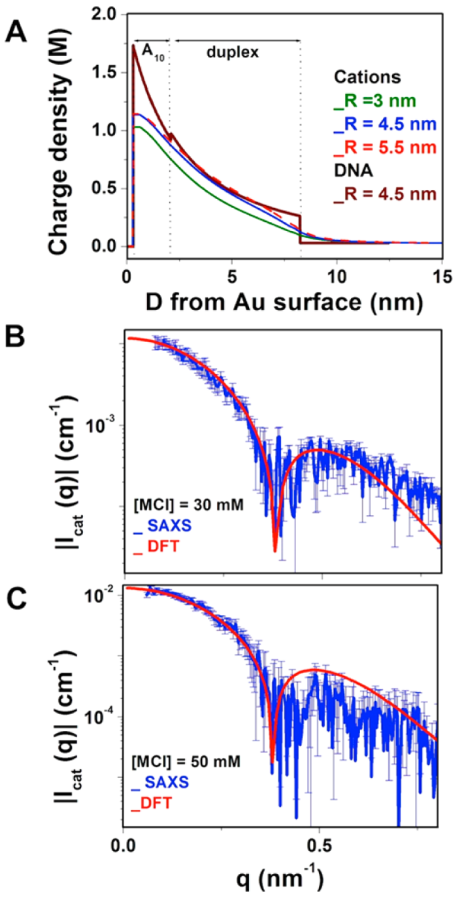

Figure 4. Comparisons of DFT-derived and SAXS-extracted cation-distribution-dependent intensities. (A) For SNA-AuNPs in 30 mM MCl, and for three different Au core sizes, the DFT-derived Na^+ distribution as a function of distance from the Au surface (green, blue, and red curves) and the DNA charge density for $R = 4.5$ nm Au core (brown curve). (B) Comparisons between the DFT-derived and the SAXS-extracted $|I_{cat}(q)|$ for SNA-AuNPs in 30 mM MCl and (C) 50 mM MCl. To match the SAXS-extracted $|I_{cat}(q)|$, the corresponding DFT-derived intensities were multiplied by 0.53. (An explanation for this scale-factor is given within the text.)

(assumed to be valid also for K^+, Rb^+, and Cs^+ under the heavy ion replacement approach) surrounding SNA-AuNPs as a function of the distance from the Au surface, for three different Au core sizes and for 30 mM NaCl. The effective radius for solvated Na^+ is taken to be 0.3 nm, similar to that in ref 9. Additionally, we assume an oligonucleotide shell thickness t_{DNA} = 8.2 nm (Table 1) and a maximum loading of oligonucleotides on Au nanoparticles, described above. The lengths for the oligonucleotide shell components, namely, the propyl-thiol linker, the A_{10} single stranded spacer, and the 18 base pair duplex (Figure 1A and Methods and Materials), are chosen to be $D_{th} = 0.3$ nm, $L_{ss} = 1.8$ nm, and $L_{ds} = 6.1$ nm, respectively. $L_{ds} = 6.1$ nm corresponds to an average rise per base pair of 0.34 nm, similar to the B-conformation of DNA in bulk solutions,[22] implying that the double-stranded oligonucleotide segments are radially pointing outward. The assumption regarding L_{ds} is appropriate because of the large persistence length (~50 nm) of double-stranded DNA in salt solutions.[23] The resulting DNA charge density for Au core of radius of 4.5 nm is shown in Figure 4A. The key features of the DFT derived cation distribution profiles are described briefly. Figure 4A shows that the modulations in n_{+DFT} are smeared in contrast to the corresponding sharp changes in the oligonucleotide charge density. This is because entropic forces oppose sharp discontinuities in the cation distribution. Further, despite Au-size-dependent differences in the cation distribution profiles (Figure 4A), the fraction of oligonucleotide charge that is compensated by the cations is nearly independent of the Au core size. In particular, within the SNA shell thickness t_{DNA}, the cations compensate 87% (±3%) of the oligonucleotide charge for SNA-AuNPs in 30 mM as well as 50 mM salt solutions. Finally, we note that the cation density reaches the bulk solution density at a distance ~3 nm outside the SNA shell (Figure 4A). This is because the SNA-AuNP charge is not fully compensated by the counterions. The spatial extent of excess cation density beyond the SNA shell is qualitatively consistent with the Debye length of $\kappa^{-1} = 1.75$ nm for 30 mM MCl solutions. Such DFT-derived cation distribution profiles in conjunction with SNA-AuNP characteristics (Table 1) are used to compute the theoretical polydispersity-averaged cation distribution dependent intensities $I_{cat}(q)$. Specifically, for Au core radii ranging from 2.6 to 7.0 nm, we calculate $F_{np}(q)$ by assuming the best-fit values for t_{DNA} and ρ_{DNA} for the DNA (Table 1) and by taking into account the Au size-dependent variations in DNA coverage, described above. The Au radius was changed with a step size of ~0.126 nm. The calculations use the core−shell model described in the SI. For each Au core size, the corresponding Fourier transforms of the cation distributions, *i.e.*, $\nu(q)$, are obtained from the DFT calculations (examples are shown in Figure 4A). For polydispersity-averaging of $I_{cat}(q)$, the weighted sum of the products $2F_{np}(q)\nu(q)$ is computed. The probability of the occurrence of a Au particle of a given radius is calculated from a Schulz distribution (e.g., Figure 3, inset), which is based on the mean sizes and the polydispersities in Table 1.

Figure 4B−C shows comparisons between the DFT-based and SAXS-extracted $|I_{cat}(q)|$ for SNA-AuNPs in 30 and 50 mM salt solutions, respectively. It should be noted that, despite having two different concentrations, the two data sets serve as only a test for reproducibility in the experimental $I_{cat}(q)$ (Figure S5, SI). This is because no significant changes are expected or observed for the cases of 30 and 50 mM salt concentrations (SI). The key observation from Figure 4B−C is that, for both cases, reasonable shape agreement between the experimental and the theoretical intensity profiles is found. This observation implies that the distribution of cations surrounding SNA-AuNPs have the same shapes as the DFT-derived $n_{+DFT}(r)$, which are

based on the oligonucleotide model, described above. This observation also provides information on the DNA-conformation (discussed below). However, to quantitatively match the experimental $I_{cat}(q)$, the DFT-derived intensity profiles for both concentrations were multiplied by a scale factor SF = 0.53 ± 0.07. The scale factor suggests that, in contrast to DFT, the SAXS-derived intensity $I_{cat}(q)$ corresponds to an *apparent* lower total number of cations in the oligonucleotide shell. We argue that the scale factor SF is likely due to unaccounted cation hydration effects and not due to a reduced number of cations in the SNA shell. In particular, three factors that should be considered as causes for this SF are: (1) DNA coverage reduction, (2) duplex melting, and (3) cation hydration. The first two factors would cause the total number of cations in the DNA shell to be diminished, whereas the third effect would not cause the number of cations to be reduced but could cause the effective scattering power Δf_M for each cation to be reduced. Previous studies on DNA-loading calibration[17] suggest that reduced DNA coverage should not be the likely cause for the observed SF. Furthermore, fitting of SAXS-extracted $[F_{np}(q)]^2$, under the "maximum-loading" assumption, yields reasonable values for t_{DNA} and ρ_{DNA}, which correctly predict the effective number of electrons for the oligonucleotides (SI). Therefore, the "maximum-loading" assumption is reasonable. Duplex dehybridization can also be ruled out, since the melting temperature for these duplexes is estimated to be $T_m \sim 50$ °C (SI), well above room temperature (RT).[24,25] However, cation hydration effects have been previously measured in an ASAXS–HIRSAXS combined study for the counterion distribution around short synthetic oligonucleotides.[10] Their study showed a reduction of 20% in Δf_{Na} and 50% in Δf_{Rb}, which in light of the uncertainties of these measurements is comparable to our ~50% average scale-factor derived from a combined DFT–HIRSAXS analysis. Their paper argued that a reduction in Δf_M should be expected for the M^+ cations used in our study, and in general for all ions that are chaotropic (have a disordered hydration shell).[26] These observations suggest that hydration reduces the effective scattering power from our M^+ cations. The reductions in Δf_M for cations can fully explain the observed scale factors in $I_{cat}(q)$. Recall that the cation profile dependent intensities $I_{cat}(q)$ are extracted from the slopes of the scattered intensity $\Delta I_M(q)$ *vs* the scattering power Δf_M of the cations. Therefore, a 50% reduction in Δf_M would cause $I_{cat}(q)$ to double. Thus we tentatively conclude that our HIRSAXS measurements agree with the DFT calculations for the cation radial distributions in both shape and absolute magnitude.

The above observations show that the DFT-derived $n_{+DFT}(r)$ are adequate descriptions of the cation distribution surrounding SNA-AuNPs. Note that DFT calculations are only for Na^+ distributions, whereas SAXS-derived $I_{cat}(q)$ are obtained from a combined analysis of SNA-AuNPs in four different salt solutions; NaCl, KCl, RbCl, and CsCl. Furthermore, a similar good match between SAXS- and DFT-derived $I_{cat}(q)$ was observed for cases where the theoretical intensities were calculated with Na^+ effective radius of either 0.1 or 0.2 nm (Figure S6, SI). These observations again validate the underlying HIR-SAXS assumption; namely, that the distribution of monovalent counterions surrounding the SNA-AuNP does not depend strongly on the ion size.

Within our experimental spatial-resolution, the DFT-derived $n_{+DFT}(r)$ is consistent with our HIRSAXS results. Figures S7–S9 show that other suitable models will only have subtle differences from the above-described DFT-derived cation distribution. We therefore can use our DFT model (Figure 4) to extract three key features:

(1) *The thickness of the SNA shell is ~8.2 nm, the average rise per base for the ss-DNA segment is ~0.18 nm, and the rise per base pair for the duplexed segment is ~0.34 nm*. The SAXS intensities calculated with cation distributions based on this DNA conformation best fit the experimental $I_{cat}(q)$ (Figure S9 and accompanying text, SI). Even ~1 nm deviations in the thickness of oligonucleotide shell or the length of the duplexed segments lead to simulated intensities that do not match the SAXS-extracted $I_{cat}(q)$ (Figures S8B,C). These observations are based on a systematic analysis of cation distribution, and hence the DNA conformations that can describe the experimental cation-dependent intensity. Specifically, we simulated $I_{cat}(q)$ by varying L_{ss} from 1.0 to 3.4 nm with a 0.2 nm step and L_{ds} from 3.6 to 6 nm with a 0.4 nm step. Additional calculations with L_{ds} = 6.1 nm, which corresponds to 0.34 nm rise/base-pair, similar to B-DNA,[22] were also performed (Figure S9). Reasonable match with SAXS-extracted $I_{cat}(q)$ were obtained for $L_{ss} = 1.8^{+0.4}_{-0.4}$ nm, $L_{ds} = 6.1^{+0.0}_{-0.9}$ nm, and thickness of the oligonucleotide shell $t_{DNA} = 8.2^{+0.4}_{-0.9}$ nm. Thus, the experimental $I_{cat}(q)$, even over the limited q-range (≤ 0.8 nm^{-1}), senses with an accuracy of ~1 nm: the thickness of the oligonucleotide shell, the length of the A_{10} single-stranded segment, and the length of the duplexed segment. The uncertainties in the DNA conformation likely arise from our limited experimental resolution but may also reflect the size fluctuation of the SNA shell. This issue is important, but beyond the scope of the present work. Future experiments with polyvalent nucleic acids,[27] which are SNAs without Au core should allow direct measurement of the SNA form factor. Such experiments along with the use of high-resolution DNA models[25,28] may shed light on this issue. Nevertheless, for the present case, we note that the observed L_{ss} and L_{ds} correspond to a $0.18^{+0.04}_{-0.04}$ nm rise per base in the single-stranded A_{10} segment and a $0.34^{+0.0}_{-0.05}$ nm rise per base-pair for the duplex segment of the oligonucleotide. Note that the best match rise per base pair for the duplexed segment corresponds to the B-DNA conformation.

The HIRSAXS-derived DNA conformation suggests a possible origin for the average rise per base or base pair of 0.26−0.28 nm observed in SNA-AuNP assemblies.[20,21] Notably, the reduction in the oligonucleotide length as compared to the B-DNA arises in part due to a reduction in the projected length of the ss-DNA segment along the surface normal. This argument is consistent with the known rigidities of ss-DNA and ds-DNA in salt solutions. In particular, at high salt concentrations such as 500 mM (see below), the persistence length for ss-DNA is expected to be less than 1 nm,[29] as compared to the persistence length of ∼50 nm for ds-DNA.[23] It should be noted that there have been no prior experiments or conclusive theoretical models[22] explaining the DNA conformation in the SNA-AuNP systems. The observations presented here should provide guidelines for refining the theoretical models for DNA conformation in various SNA-AuNP systems.

(2) *Within the SNA shell, the monovalent cations compensate ∼87% of the oligonucleotide charge.*

(3) *For the SNA-AuNPs used in the study, the average cation concentration in the SNA shell is ∼450 mM. The cation concentrations near the Au core and near the outer periphery of the SNA-AuNP are ∼1150 mM and ∼140 mM, respectively*. For the specific case of Au cores with $R = 4.5$ nm (the mean size), oligonucleotides with 46 bases per strand, and a SNA-shell thickness of 8.2 nm, the DFT-derived 87% charge compensation corresponds to an average cation concentration of ∼450 mM in the SNA shell. This implies that the average cation density in the SNA shell is ∼15× and ∼9× higher than the bulk-solution cation concentrations of 30 mM and 50 mM, respectively. Based on the DFT analysis of the HIRSAXS data, for SNA-AuNPs with small Au cores ($R \leq 10$ nm), an empirical formula for the average cation concentration in the SNA shell can be derived: $\langle M^+ \rangle(R) = C[N_{DNA}(R)((N_b + 2N_{bp})/0.6023V_{sh})]$, where $C = 0.87$ is the DFT-derived extent of oligonucleotide charge compensated by cations. The multiplicative factor 0.6023 converts the concentration to mol/L. $N_{DNA}(R)$ is the DNA loading on the AuNPs (Figure S4B), N_b is the number of bases in a single-strand segment, N_{bp} is the number of base-pairs in the duplexed segment of the oligonucleotide, and V_{sh} is the volume of the SNA shell. Figure 4A also shows that, for such SNA-AuNPs, the cation concentration is ∼1150 mM close to the Au core surface, which is ∼38× and ∼23× higher than the cation concentrations of 30 nM and 50 mM, respectively, in the bulk solution. Another region of interest is the SNA-AuNP outer periphery, where the SNAs interact with the surrounding environment. For example, proteins in a cellular environment or other SNA-AuNPs in the formation of crystalline SNA-AuNP assemblies.[30,31] Based on Figure 4A, the cation concentration at the outer periphery of the SNA-AuNPs is ∼140 mM, corresponding to ∼5× and ∼3× enhancements over the bulk concentrations of 30 and 50 mM, respectively.

CONCLUSIONS

To summarize, we have probed the distribution of monovalent cations surrounding SNA-AuNPs by a combined HIRSAXS-DFT approach. This approach yielded key insights into the cation distribution and the DNA conformation. In particular, an average enhancement of ∼15× and ∼9× in the local cation concentration was observed for SNA-AuNPs in of 30 mM and 50 mM salt solutions, respectively. Furthermore, the cation distribution was found to be nonuniform, directly dependent on the radial charge distribution of oligonucleotides and with an overall extent corresponding to the approximate oligonucleotide shell thickness $t_{DNA} \sim 0.3 + 0.18 \times N_b + 0.34 \times N_{bp}$ (nm), where 0.3 nm is the length of the thiol linker, N_b is the number of bases in the single-stranded segment, and N_{bp} is the number of base-pairs in the duplexed segment of the oligonucleotide strand capping the Au core. Our studies also demonstrate the feasibility of HIRSAXS in probing the monovalent counterion distribution around electron-dense colloids such as polyelectrolyte coated metal (for example, Au, Ag) nanoparticles.

The results presented here should be useful for studies aimed at explaining the effects of high local counterion concentrations, such as the stability of SNA-AuNPs against degradation by nucleases,[7] as well as the conformation of oligonucleotides in SNA-AuNPs.[22] A worthy extension of the current study would be to test the validity of the heavy ion replacement approach for the distribution of multivalent cations surrounding SNA-AuNPs.

MATERIALS AND METHODS

Samples. To demonstrate reproducibility, we performed two separate experiments on two separate sample sets. All DNA strands were synthesized on a MM48 DNA synthesizer (BioAutomation) using reagents from Glen Research. Two oligonucleotide sequences were utilized: a thiol-modified strand that was covalently attached to the surface of the gold nanoparticle (sequence: 5′-AACAATTATACTCAGCAAAAAAAAAAAA-C_3SH-3′, where C_3SH denotes a propyl-thiol modification), and a complementary strand that hybridized to the thiol-modified strand to create a DNA duplex (sequence: 5′-TTGCTGAGTATAATTGTT-3′). Both of these sequences have been used previously[32] and exhibit no off-target effects such as mismatched hybridization or particle instability. Au nanoparticles from TedPella were used without further purification or treatment. Thiol-modified oligonucleotides were attached to the Au nanoparticles per literature precedent[18] to achieve maximum DNA loading. A high density of DNA coverage on the Au nanoparticles was qualitatively inferred during the functionalization process. Specifically, the DNA functionalization process for synthesizing the SNA-AuNPs required incubating the nanoparticles

in high salt concentrations. If the DNA density was indeed significantly low, the particles would not be stable at these elevated salt concentrations. Since no aggregation was observed during the particle preparation process, the nanoparticles must have high DNA coverage. Prior to SAXS measurements, the DNA-functionalized nanoparticles were combined with the complementary strand at a ratio of 60 complements per nanoparticle in the appropriate salt solution (MCl, M = Na^+, K^+, Rb^+, Cs^+). Salt concentrations of 30 and 50 mM were chosen because for these concentrations significant contrast between the cation concentration in the SNA shell and the bulk solutions is expected. Further, at these low salt concentrations, no aggregation of SNA-AuNPs is expected, ensuring that the SNA-AuNP solutions were uniform dispersions of isolated nanoparticles.

X-ray Analysis. SAXS measurements were carried out at beamline 5ID-D[33] of the Advanced Photon Source. To avoid strong fluorescence from the Au cores, X-ray energy was tuned to 11.5 keV (λ = 0.108 nm), which is below the L absorption edges for Au (11.9−14.3 keV). The X-ray spot size at the sample position was ~0.25 mm, and the incident flux was ~8×10^{11} photons/s. For normalizing the scattered intensities, the incident X-ray flux and the transmitted intensities were monitored by an ion chamber just before the flow-cell and a cadmium tungstate scintillating crystal and a pin diode embedded in the beam stop just before a Mar165 2D detector used for collecting the SAXS patterns. To avoid air scattering, we used an in-vacuum flow cell to enclose the capillary tube.[33] For a given salt concentration, the same capillary tube was used for all measurements. The beam paths were also under vacuum during the measurements. To reduce radiation damage, during measurements, the sample solutions were continuously flowed through the capillary tube. All measurements were performed at room temperature. SNA-AuNP aggregation or sticking of SNA-AuNPs to the capillary walls was not observed for the salt concentrations used. However, as a precautionary step, the capillary was washed by using an iodine solution (for dissolving any residual AuNPs), an aqueous solution of sodium dodecyl sulfate (SDS) and copious amounts (~10 mL) of pure water after each set of measurements. Furthermore, before each new measurement, the SAXS from capillary, empty and with pure water, were taken to ensure that the background signal did not change between measurements. A zero beam detector signal was also collected and appropriately subtracted from the measured scattered intensity. For SNA-AuNP samples, the exposure time for each measurement was 0.5 s, and five sets of scattering data were collected per sample. Azimuthal integration of the 2D SAXS profiles (using Fit 2D) yielded the 1D intensity profile $I(2\theta)$. Similarly, with 10 s exposure, five sets of scattering data were collected from empty capillary and MCl (M = Na, K, Rb, or Cs) salt solutions (without SNA-AuNPs) for background subtraction and from pure water for converting the intensities on the absolute scale, following standard procedures.[34] Specifically, pure water scattering and salt solution scattering (after capillary scattering subtraction) were nearly flat for $q > 0.15$ nm^{-1}. For conversion to an absolute intensity scale, or more precisely, a differential scattering cross-section per unit volume, the intercept of the best-fit line through the near constant water scattering was set at 0.0165 cm^{-1}, and all subsequent data was scaled accordingly.[34] The scattering from the salt solutions was only slightly higher than that for pure water (e.g., by ~0.001 cm^{-1} for 50 mM RbCl). By contrast, the scattering from SNA-AuNPs in 30 mM NaCl (*e.g.*) varied from 9.26 to 0.22 cm^{-1}, over a q-range of ~0.07−0.8 nm^{-1}. The background-subtracted data on the absolute intensity scales shown are the average of the five measurements for each sample. To account for small differences in the SNA-AuNP concentrations in different MCl solutions, the SAXS intensities $\Delta I_M(q)$ were rescaled (Figures S10−S11).

DFT. Within the framework of classical DFT, we derive the Boltzmann distributions of salt ions surrounding a single SNA-AuNP by a functional minimization of the grand potential functional:

$$\beta\Omega[\{n\}] = \beta\Omega_{id}[\{n\}] + \frac{1}{2}\int d\mathbf{r}\phi(\mathbf{r})Q(\mathbf{r}) + \beta\Omega_{exc}^{CS}[\{n\}] \quad (4)$$

that includes the ideal gas contribution

$$\beta\Omega_{id}[\{n\}] = \sum_{\alpha=+,-}\int d\mathbf{r} n_\alpha(\mathbf{r})\left(\ln\frac{n_\alpha(\mathbf{r})}{n_s} - 1\right) \quad (5)$$

where n_s is the salt concentration in the bulk solution. A local density approximation is made for the hard core excess free energy, derived from the Carnahan−Starling excess free energy for a homogeneous system of hard spheres,

$$\beta\Omega_{exc}^{CS}[\{n\}] = \int d\mathbf{r} n(\mathbf{r})\frac{4\eta(\mathbf{r}) - 3\eta^2(\mathbf{r})}{[1-\eta(\mathbf{r})]^2} \quad (6)$$

where $n = n_+ + n_-$ is the total density of ions, $\eta = v_p n$ is the total volume fraction of salt, and v_p is the particle volume. The electrostatic contribution is accounted for by a self-consistent field ϕ,

$$\phi(\mathbf{r}) = \int d\mathbf{r}' \frac{l_B Q(\mathbf{r}')}{|\mathbf{r}-\mathbf{r}'|} \quad (7)$$

that satisfies Poisson's equation, where $Q = n_+ - n_- + n_{DNA}$ is the total charge, and n_{DNA} is a fixed charge density imposed by the oligonucleotide linkers. The linkers are considered to be stiff. The Boltzmann distributions of ions derived from eq 4 are

$$n_\pm = n_s \exp(\mp\phi(\mathbf{r}) - \mu_{exc}^{CS}[n]) \quad (8)$$

that are solved self-consistently with eq 7 in a conical unit cell that contains exactly one oligonucleotide linker. The apex of the cell is located at the center of the Au core, and the axis of the cone coincides with the direction of the linker, as described in detail in ref 9. At the boundary of the unit cell, we impose the conditions

$$\lim_{r\to\infty}\frac{\partial\phi(r,\theta)}{\partial r} = \lim_{r\downarrow a}\frac{\partial\phi(r,\theta)}{\partial r} = 0,$$
$$\lim_{\theta\uparrow\theta_m}\frac{\partial\phi(r,\theta)}{\partial r} = \lim_{\theta\downarrow 0}\frac{\partial\phi(r,\theta)}{\partial r} = 0 \quad (9)$$

which guarantee global charge neutrality. Here, a is the minimal distance of an ion to the center of the Au core, and θ_m is the angle between the surface of the cell and the central axis set by the total surface density of linkers. To account for cation hydration the size of Na^+ ions in the DFT calculations is chosen to be 0.3 nm. With a spatial resolution of 0.1 Å, we evaluate the azimuthally averaged ion concentrations for core radii between 2.6 and 7.0 nm using the maximal grafting density determined from Figure S4. The entire set of calculations are performed within ~20 min on a single CPU.

Conflict of Interest: The authors declare no competing financial interest.

Acknowledgment. S.K., R.J.M., M.O.d.I.C., C.A.M., and M.J.B. were funded by AFOSR (FA9550-11-1-0275), J.W.Z. by AFOSR (FA9550-10-1-0167), and C.-Y.L. by DOE-BES DE-FG02-08ER46539. The SAXS experiments were performed at the Advanced Photon Source (APS) 5ID-D beamline of DND-CAT, which is supported through E. I. duPont de Nemours & Co., Northwestern University, The Dow Chemical Co., and the NSF funded MRSEC at NU. Use of the APS was supported by DOE-BES (DE-AC02-06CH11357). We thank S. Weigand of DND-CAT for assistance with the SAXS setup.

Supporting Information Available: (1) Model ASAXS calculations and description of the model for SNA-AuNP structural characterizations. (2) DFT calculations showing the effect of cation size on their distribution around SNA-AuNPs. (3) SAXS-extracted $I_{cat}(q)$ over an extended q-range. (4) Estimation of the number of oligonucleotides SNA-AuNP. (5) Effect of cation size on the simulated SAXS intensity $I_{cat}(q)$. (6) Effect of salt concentration on SAXS intensity $I_{cat}(q)$. (7) Geometric models for cation distribution surrounding SNA-AuNPs. (8) Detailed analysis of DNA conformations. (9) Data processing (10) Melting temperature for DNA duplexes. This material is available free of charge *via* the Internet at http://pubs.acs.org.

REFERENCES AND NOTES

1. Mirkin, C. A.; Letsinger, R. L.; Mucic, R. C.; Storhoff, J. J. A DNA-Based Method for Rationally Assembling Nanoparticles into Macroscopic Materials. *Nature* **1996**, *382*, 607–609.
2. Giljohann, D. A.; Seferos, D. S.; Daniel, W. L.; Massich, M. D.; Patel, P. C.; Mirkin, C. A. Gold Nanoparticles for Biology and Medicine. *Angew. Chem., Int. Ed.* **2010**, *49*, 3280–3294.
3. Cutler, J. I.; Auyeung, E.; Mirkin, C. A. Spherical Nucleic Acids. *J. Am. Chem. Soc.* **2012**, *134*, 1376–1391.
4. Macfarlane, R. J.; O'Brien, M. N.; Petrosko, S. H.; Mirkin, C. A. Nucleic Acid-Modified Nanostructures as Programmable Atom Equivalents: Forging a New "Table of Elements". *Angew. Chem., Int. Ed.* **2013**, *52*, 5688–5698.
5. Lytton-Jean, A. K. R.; Mirkin, C. A. A Thermodynamic Investigation into the Binding Properties of DNA Functionalized Gold Nanoparticle Probes and Molecular Fluorophore Probes. *J. Am. Chem. Soc.* **2005**, *127*, 12754–12755.
6. Rosi, N. L.; Giljohann, D. A.; Thaxton, C. S.; Lytton-Jean, A. K. R.; Han, M. S.; Mirkin, C. A. Oligonucleotide-Modified Gold Nanoparticles for Intracellular Gene Regulation. *Science* **2006**, *312*, 1027–1030.
7. Seferos, D. S.; Prigodich, A. E.; Giljohann, D. A.; Patel, P. C.; Mirkin, C. A. Polyvalent DNA Nanoparticle Conjugates Stabilize Nucleic Acids. *Nano Lett.* **2009**, *9*, 308–311.
8. Jin, R. C.; Wu, G. S.; Li, Z.; Mirkin, C. A.; Schatz, G. C. What Controls the Melting Properties of DNA-Linked Gold Nanoparticle Assemblies? *J. Am. Chem. Soc.* **2003**, *125*, 1643–1654.
9. Zwanikken, J. W.; Guo, P.; Mirkin, C. A.; Olvera de la Cruz, M. Local Ionic Environment around Polyvalent Nucleic Acid-Functionalized Nanoparticles. *J. Phys. Chem. C* **2011**, *115*, 16368–16373.
10. Das, R.; Mills, T. T.; Kwok, L. W.; Maskel, G. S.; Millett, I. S.; Doniach, S.; Finkelstein, K. D.; Herschlag, D.; Pollack, L. Counterion Distribution around DNA Probed by Solution X-Ray Scattering. *Phys. Rev. Lett.* **2003**, *90*, 188103.
11. Andresen, K.; Das, R.; Park, H. Y.; Smith, H.; Kwok, L. W.; Lamb, J. S.; Kirkland, E. J.; Herschlag, D.; Finkelstein, K. D.; Pollack, L. Spatial Distribution of Competing Ions around DNA in Solution. *Phys. Rev. Lett.* **2004**, *93*, 248103.
12. Dingenouts, N.; Merkle, R.; Guo, X.; Narayanan, T.; Goerigk, G.; Ballauff, M. Use of Anomalous Small-Angle X-Ray Scattering for the Investigation of Highly Charged Colloids. *J. Appl. Crystallogr.* **2003**, *36*, 578–582.
13. Dingenouts, N.; Patel, M.; Rosenfeldt, S.; Pontoni, D.; Narayanan, T.; Ballauff, M. Counterion Distribution around a Spherical Polyelectrolyte Brush Probed by Anomalous Small-Angle X-Ray Scattering. *Macromolecules* **2004**, *37*, 8152–8159.
14. Goerigk, G.; Schweins, R.; Huber, K.; Ballauff, M. The Distribution of Sr^{2+} Counterions around Polyacrylate Chains Analyzed by Anomalous Small-Angle X-Ray Scattering. *Europhys. Lett.* **2004**, *66*, 331–337.
15. Pabit, S. A.; Meisburger, S. P.; Li, L.; Blose, J. M.; Jones, C. D.; Pollack, L. Counting Ions around DNA with Anomalous Small-Angle X-Ray Scattering. *J. Am. Chem. Soc.* **2010**, *132*, 16334–16336.
16. Als-Nielsen, J.; McMorrow, D. *Elements of Modern X-Ray Physics*, 2nd ed.; John Wiley: Chichester, U.K., 2011.
17. Hill, H. D.; Millstone, J. E.; Banholzer, M. J.; Mirkin, C. A. The Role Radius of Curvature Plays in Thiolated Oligonucleotide Loading on Gold Nanoparticles. *ACS Nano* **2009**, *3*, 418–424.
18. Hurst, S. J.; Lytton-Jean, A. K. R.; Mirkin, C. A. Maximizing DNA Loading on a Range of Gold Nanoparticle Sizes. *Anal. Chem.* **2006**, *78*, 8313–8318.
19. Putnam, C. D.; Hammel, M.; Hura, G. L.; Tainer, J. A. X-Ray Solution Scattering (SAXS) Combined with Crystallography and Computation: Defining Accurate Macromolecular Structures, Conformations and Assemblies in Solution. *Q. Rev. Biophys.* **2007**, *40*, 191–285.
20. Macfarlane, R. J.; Jones, M. R.; Senesi, A. J.; Young, K. L.; Lee, B.; Wu, J.; Mirkin, C. A. Establishing the Design Rules for DNA-Mediated Colloidal Crystallization. *Angew. Chem., Int. Ed.* **2010**, *49*, 4589–4592.
21. Jones, M. R.; Macfarlane, R. J.; Lee, B.; Zhang, J.; Young, K. L.; Senesi, A. J.; Mirkin, C. A. DNA-Nanoparticle Superlattices Formed from Anisotropic Building Blocks. *Nat. Mater.* **2010**, *9*, 913–917.
22. Lee, O.-S.; Prytkova, T. R.; Schatz, G. C. Using DNA to Link Gold Nanoparticles, Polymers, and Molecules: A Theoretical Perspective. *J. Phys. Chem. Lett.* **2010**, *1*, 1781–1788.
23. Hagerman, P. J. Flexibility of DNA. *Annu. Rev. Biophys. Biophys. Chem.* **1988**, *17*, 265–286.
24. Baldino, F.; Chesselet, M. F.; Lewis, M. E. High-Resolution *In Situ* Hybridization Histochemistry. *Methods Enzymol.* **1989**, *168*, 761–777.
25. Freeman, G. S.; Hinckley, D. M.; de Pablo, J. J. A Coarse-Grain Three-Site-Per-Nucleotide Model for DNA with Explicit Ions. *J. Chem. Phys.* **2011**, *135*, 165104.
26. Mahler, J.; Persson, I. A Study of the Hydration of the Alkali Metal Ions in Aqueous Solution. *Inorg. Chem.* **2012**, *51*, 425–438.
27. Cutler, J. I.; Zhang, K.; Zheng, D.; Auyeung, E.; Prigodich, A. E.; Mirkin, C. A. Polyvalent Nucleic Acid Nanostructures. *J. Am. Chem. Soc.* **2011**, *133*, 9254–9257.
28. Hinckley, D. M.; Freeman, G. S.; Whitmer, J. K.; de Pablo, J. J. An Experimentally-Informed Coarse-Grained 3-Site-Per-Nucleotide Model of DNA: Structure, Thermodynamics, and Dynamics of Hybridization. *J. Chem. Phys.* **2013**, *139*, 144903–144903.
29. Tinland, B.; Pluen, A.; Sturm, J.; Weill, G. Persistence Length of Single-Stranded DNA. *Macromolecules* **1997**, *30*, 5763–5765.
30. Nykypanchuk, D.; Maye, M. M.; van der Lelie, D.; Gang, O. DNA-Guided Crystallization of Colloidal Nanoparticles. *Nature* **2008**, *451*, 549–552.
31. Park, S. Y.; Lytton-Jean, A. K. R.; Lee, B.; Weigand, S.; Schatz, G. C.; Mirkin, C. A. DNA-Programmable Nanoparticle Crystallization. *Nature* **2008**, *451*, 553–556.
32. Macfarlane, R. J.; Lee, B.; Jones, M. R.; Harris, N.; Schatz, G. C.; Mirkin, C. A. Nanoparticle Superlattice Engineering with DNA. *Science* **2011**, *334*, 204–208.
33. Weigand, S.; Stillwell, B.; Guise, W. E.; Quintana, J. P. G.; Keane, D. T. Flexibility and High Throughput: Supporting SAXS Users at a Joint Industrial Academic Beamline. *Adv. X-Ray Anal.* **2009**, *52*, 58–68.
34. Fan, L.; Degen, M.; Bendle, S.; Grupido, N.; Ilavsky, J. The Absolute Calibration of a Small-Angle Scattering Instrument with a Laboratory X-Ray Source. *J. Phys.: Conf. Ser.* **2010**, *247*, 012005.